Dynamic Decoupling Current Control of Boost and Buck Multiple Converters

Toshiyuki Fujita, *Member, IEEE*, Masahiro Mae, *Member, IEEE*, Hiroshi Fujimoto, *Fellow, IEEE*,
Michihiro Nakagawa, Yoshiki Yasuda, and Akio Yamagiwa

***Abstract*—A dc–dc converter is widely used in various applications for energy conversion systems. This article focuses on a home energy management system that uses boost and buck converters connected to the same dc link voltage, treating the system as a multiinput multioutput (MIMO) system. A state-space averaging model analysis is used to model the system. The proposed dynamic current decoupling control compensates the dc link voltage at each input. The proposed approach calculates that the elements of the off-diagonal terms become zero. The diagonal terms are first-order systems. The model analysis suggests that the compensation of the duty error needs to be stable in the dc link voltage. The experimental test bench system is constructed and tested to verify the proposed control. By system identification, the model represents the major dynamics of the actual system. Nyquist stability analysis for the MIMO system depicts that the conventional control might be unstable due to MIMO interaction. Step responses also verify that the proposed control suppresses the overshoot voltage and converges faster compared to conventional voltage control.**

***Index Terms*—Current control, dc-dc power converters, decoupling control, multiinput multioutput (MIMO), Nyquist stability analysis, voltage control.**

I. INTRODUCTION

DC–DC converters are widely used in dc microgrids, photovoltaics (PV) converters, and battery chargers. In addition, power electronics progress integration, miniaturization, and enable high efficiency. Multiple converters are connected to the same dc bus to reduce cost and increase efficiency. This configuration is seen in many applications, such as dc microgrids [1], ships [2], electric vehicle (EV)s [3], data centers, and home energy management systems (EMSs) [4].

The EMS is composed of many converters, which include the home EMS [5], building EMS [6], factory EMS [7], and a vehicle to home application [8]. These EMSs optimize the balance of the power demand and supply between subsystems, which consist of renewable energy sources, such as PV and wind turbines, battery storage, and the grid. Designing and testing the system of multiple converters individually takes time. However, the development speed is accelerating as the sector coupling of EMSs increases. To solve this problem, the power electronics building block (PEBB) has been proposed [9]. PEBB integrates power devices, gate drivers, sensors, etc. toward plug-and-play power electronics. PEBB also reduces cost, time, and maintenance, and enables integration. PEBB is adapted to a variety of applications, such as high (medium) grid voltage [10], wireless power transfer [11], aircraft propulsion [12], DAB converter [13], and EMSs [14]. Since their systems are multiinput multioutput (MIMO) systems, a controller is designed or analyzed as a single-input single-output (SISO) system, considering interferences between converters as a disturbance or feedforward signal.

A constant power load (CPL) (e.g., a motor drive) is often connected to the dc bus of a system. When the CPL subsystem increases in input voltage, the input current decreases and vice versa [3], which results in a negative incremental impedance. This CPL generates limit cycles, which increase current and voltage ripples and cause semiconductor device degradation. Many methods have been proposed to resolve this voltage instability. Nonlinear PWM control has been introduced in [15], which is based on the estimation of output power. Passivity-based control has been developed to stabilize the dc link voltage and combine the disturbance observer, i.e., nonlinear observer [16] and extended Kalman filter [17]. Another approach is an impedance specification method of parameter-based Bode and Nyquist plot [18]. However, the experimental approaches to the instability have not yet been clarified and these methods are focused on a single converter for the improvement of followability.

Droop control offers absolute stability as long as its gain remains within stable operating boundaries, which is widely used in grid-connected systems. Its stability for ac grid-connected inverters has been analyzed [19]. Despite its robustness, droop control is unsuitable for precise current control because it inherently contains an error with respect to the command value; even at exceptionally high gains, it consistently results in residual errors in the command value after the system converges.

There are several applications of research using MIMO theory. Two-input-two-output torque difference amplification motor drive system of electrified vehicles installs a summation-differential mode transformation, which suppresses the vibration

Received 21 April 2025; revised 9 July 2025; accepted 11 August 2025. Date of publication 19 August 2025; date of current version 13 November 2025. This work was supported by the JSPS KAKENHI under Grant JP24K17256. Recommended for publication by Associate Editor D. O. Neacsu. *(Corresponding author: Toshiyuki Fujita.)*

Toshiyuki Fujita and Hiroshi Fujimoto are with the Graduate School of Frontier Sciences, the University of Tokyo, Kashiwa City 277-8561, Japan (e-mail: t-fujita@edu.k.u-tokyo.ac.jp).

Masahiro Mae is with the Graduate School of Engineering, the University of Tokyo, Bunkyo-ku 113-8656, Japan.

Michihiro Nakagawa, Yoshiki Yasuda, and Akio Yamagiwa are with Technology and Innovation Center, DAIKIN INDUSTRIES, Ltd., Settsu 566-8585, Japan.

Color versions of one or more figures in this article are available at https://doi.org/10.1109/TPEL.2025.3600009.

Digital Object Identifier 10.1109/TPEL.2025.3600009

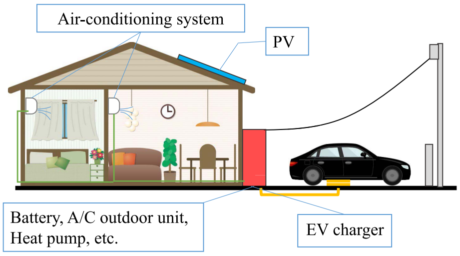

Fig. 1. Concept of our proposed EMS.

of the vehicle [20]. A semiconductor vertical furnace heats a 100 300 mm silicon wafers in the same batch on rapid and precise thermal control using frequency response data [21]. Low-noise error signals for controlling the mirror positions of gravitational wave detectors are crucial for attaining the highest possible sensitivity in the low-frequency detection range. MIMO stability analysis and decoupling matrix suppress large transients and interaction of three angles of mirror [22].

Some papers consider output decoupling for dc–dc converters. One method involves solving a nonlinear function using model predictive control [23]. Another approach achieves decoupling by installing a precompensator [24]. In addition, a MIMO converter can be controlled using sliding mode control for each current [25]. In all these cases, the effectiveness of decoupling would likely be reduced if model errors occur, and stability analysis is not discussed.

Although multiple converters are connected to a dc link, each converter causes voltage instability. Widening the control bandwidth is not an essential solution due to the interference present between converters. This article considers multiple converters combined as one system. The system is treated as a MIMO system. The main contributions of this article are as follows:

C1) Control each input independently for improved tracking performance, which does not affect other voltage outputs.

C2) Propose a system design that allows each component to be added stability as a MIMO system when adding additional components.

C3) Improve the followability desired for the input and output pair, regardless of the behavior of other inputs.

To verify the above, a system that combines a boost converter and a buck converter is designed, and the MIMO stability analysis is conducted in the Nyquist diagram with generalized Gershgorin band. The stability is confirmed using a SISO Nyquist diagram with the generalized Gershgorin bands. Also, confirmed that the current is not affected by other inputs and that the voltage is not affected by other outputs for evaluation of the four-step response.

II. MODELING AND CONVENTIONAL CONTROLLER OF MULTIPLE CONVERTER SYSTEM

Fig. 1 displays the proposed concept of an EMS. This EMS integrates systems that use relatively large-rated power (i.e., over 1 kW) of electric devices at home, such as PV panels, battery systems, air conditioners, grid-connected inverters, and EV chargers, into a single box and controls them as an integrated unit. This article aims to validate the stability and improve the responsiveness of this EMS. Generally, the PV converter is used for a buck converter and the battery converter is for a boost converter.

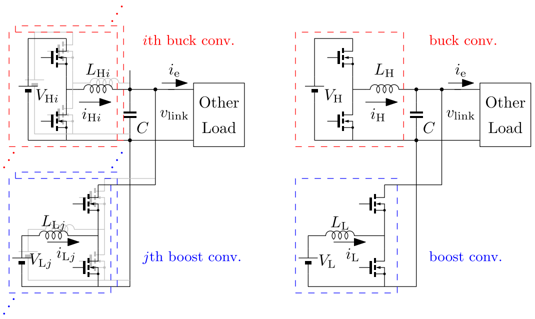

(a) (b)

Fig. 2. Circuit configuration of the multiple converter system with buck and boost converters. (a) m boost converters and n buck converters. (b) Minimum units of the multiple system are $m = 1$ and $n = 1$.

Fig. 2(a) generalizes this EMS as a system in which m boost converters, n buck converters, and other loads are connected to a dc link capacitor C whose voltage is v_{link}. The dc voltage sources of the ith buck converter, jth boost converter are defined as $V_{\mathrm{H}i}$ and $V_{\mathrm{L}j}$, respectively. Also, the inductances and parasitic resistances of the ith buck and jth boost inductors are $L_{\mathrm{H}i}$, $r_{\mathrm{H}i}$, $L_{\mathrm{L}j}$, and $r_{\mathrm{L}j}$. The disturbance current is i_{e}.

Fig. 2(b) shows the circuit configuration of the proposed system. Still, for the sake of simplicity, the system is evaluated that connects two different converters $m = 1$ and $n = 1$: one boost converter and one buck converter, as shown in Fig. 2(a). The voltages are defined high-side and low-side dc constant voltage sources and dc link voltage V_{H}, V_{L}, and v_{link}, as shown in Fig. 2. Also, the currents are high and low-side inductor and disturbance currents as i_{H}, i_{L}, and i_e, respectively. Note that small symbols represent instantaneous values and capital symbols are rms values except for constant values. The inductances and parasitic resistances of the inductors are also defined as L_{H} and L_{L}, and r_{H} and r_{L}, respectively. The converters are controlled by a synchronous rectification. This article assumes $i_e = 0$ in the analysis focused on the basic characteristics of the multiple converter system.

A. Modeling Using State-Space Averaging Method

Applying Kirchhoff's law to the system in Fig. 2(b) gives the following:

$$\frac{\mathrm{d}}{\mathrm{d}t}x = f(x) = \begin{pmatrix} \dfrac{d_{\mathrm{H}}}{L_{\mathrm{H}}}V_{\mathrm{H}} - \dfrac{r_{\mathrm{H}}}{L_{\mathrm{H}}}i_{\mathrm{H}} - \dfrac{v_{\mathrm{link}}}{L_{\mathrm{H}}} \\ -\dfrac{r_{\mathrm{L}}}{L_{\mathrm{L}}}i_{\mathrm{L}} - \dfrac{(1-d_{\mathrm{L}})}{L_{\mathrm{L}}}v_{\mathrm{link}} + \dfrac{v_{\mathrm{link}}}{L_{\mathrm{L}}} \\ \dfrac{i_{\mathrm{H}}}{C} + \dfrac{(1-d_{\mathrm{L}})}{C}i_{\mathrm{L}} - \dfrac{i_e}{C} \end{pmatrix} \tag{1}$$

$$\text{where} \quad x = \frac{\mathrm{d}}{\mathrm{d}t}\begin{pmatrix} i_{\mathrm{H}} & i_{\mathrm{L}} & v_{\mathrm{link}} \end{pmatrix}^{\mathrm{T}}.$$

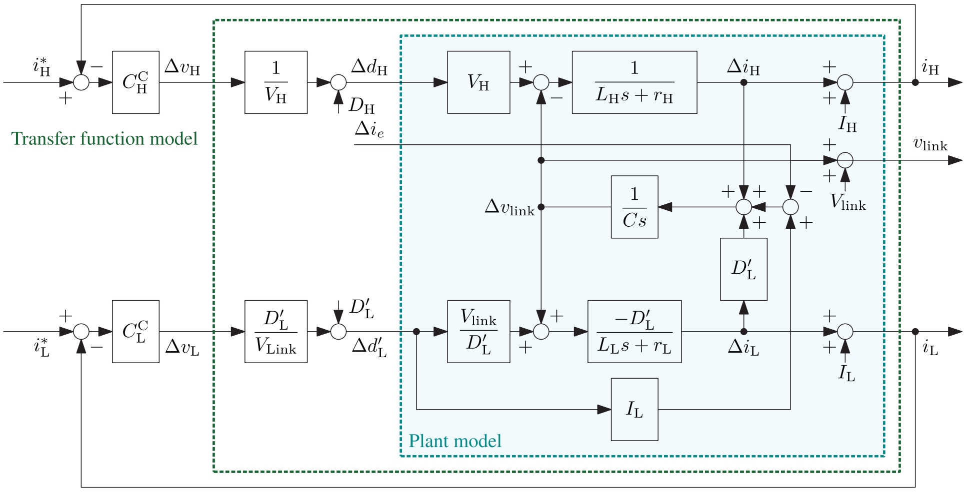

Fig. 3. Conventional control diagrams of the multiple converter system.

By linearizing (1) around the steady-state condition, small-signal response state-space representation (2) and (3) are

$$\frac{d}{dt}\Delta x = \tilde{A}\Delta x + \tilde{B}\Delta d \tag{2}$$

$$\Delta y = \tilde{C}\Delta x \tag{3}$$

$$\text{where}\quad \Delta x = \Delta y = \begin{pmatrix}\Delta i_{\mathrm{H}} & \Delta i_{\mathrm{L}} & \Delta v_{\mathrm{link}}\end{pmatrix}^{\mathrm{T}}$$

$$\tilde{A} = \frac{\partial f}{\partial x_k} = \begin{pmatrix}\frac{r_{\mathrm{H}}}{L_{\mathrm{H}}} & 0 & -\frac{1}{L_{\mathrm{H}}}\\ 0 & -\frac{r_{\mathrm{L}}}{L_{\mathrm{L}}} & -\frac{D'_{\mathrm{L}}}{L_{\mathrm{L}}}\\ \frac{1}{C} & \frac{D'_{\mathrm{L}}}{C} & 0\end{pmatrix}$$

$$\tilde{B} = \frac{\partial f}{\partial d_k} = \begin{pmatrix}\frac{V_{\mathrm{H}}}{L_{\mathrm{H}}} & 0\\ 0 & -\frac{V_{\mathrm{link}}}{L_{\mathrm{L}}}\\ 0 & \frac{I_{\mathrm{L}}}{C}\end{pmatrix}$$

$$\Delta d = \begin{pmatrix}\Delta d_{\mathrm{H}} & \Delta d'_{\mathrm{L}}\end{pmatrix}^{\mathrm{T}}$$

$$\tilde{C} = I.$$

The lower duty is defined by $d'_{\mathrm{L}} = (1 - d_{\mathrm{L}})$. The Laplace transformation of (2) are given by

$$\Delta i_{\mathrm{H}} = \frac{1}{L_{\mathrm{H}}s + r_{\mathrm{H}}}(V_{\mathrm{H}}\Delta d_{\mathrm{H}} - \Delta v_{\mathrm{link}}) \tag{4}$$

$$\Delta i_{\mathrm{L}} = -\frac{D'_{\mathrm{L}}}{L_{\mathrm{L}}s + r_{\mathrm{L}}}\left(\frac{V_{\mathrm{L}}}{D'_{\mathrm{L}}}\Delta d'_{\mathrm{L}} + \Delta v_{\mathrm{link}}\right)$$

$$\Delta v_{\mathrm{link}} = \frac{1}{sC}(\Delta i_{\mathrm{H}} + D'_{\mathrm{L}}\Delta i_{\mathrm{L}} + I_{\mathrm{L}}\Delta d'_{\mathrm{L}} - \Delta i_{\mathrm{e}}).$$

Steady-state conditions are calculated by (1) $= 0$

$$D'_{\mathrm{L}}I_{\mathrm{L}} = I_e - I_{\mathrm{H}} \tag{5}$$

$$D_{\mathrm{H}} = \frac{V_{\mathrm{link}} + r_{\mathrm{H}}I_{\mathrm{H}}}{V_{\mathrm{H}}}$$

$$D'_{\mathrm{L}} = \frac{V_{\mathrm{L}} + \sqrt{V_{\mathrm{L}}^2 - 4V_{\mathrm{link}}r_{\mathrm{L}}I_{\mathrm{L}}}}{2V_{\mathrm{link}}}.$$

B. Conventional Controller Design

Fig. 3 shows overall conventional control diagrams of the proposed system. The cyan box indicates the small-signal model of the plant. The current controllers $C_{\mathrm{H}}^{\mathrm{C}}$ and $C_{\mathrm{L}}^{\mathrm{C}}$ are proportional and integral (PI) controllers in this article. The current controllers are designed by considering the plant as a first-order system and are the pole placement detailed equations shown later in Section IV-B.

The state-space equation of the green box in Fig. 3 is expressed as

$$\frac{d}{dt}\Delta x = \tilde{A}^{\mathrm{C}}\Delta x + \tilde{B}^{\mathrm{C}}\Delta u^{\mathrm{C}} \tag{6}$$

$$\Delta y = \tilde{C}\Delta x$$

where

$$\tilde{A}^{\mathrm{C}} = \tilde{A}$$

$$\tilde{B}^{\mathrm{C}} = \begin{pmatrix}\frac{1}{L_{\mathrm{H}}} & 0\\ 0 & -\frac{1}{L_{\mathrm{L}}}\\ 0 & \frac{I_{\mathrm{L}}}{CV_{\mathrm{link}}}\end{pmatrix}$$

$$\Delta u^{\mathrm{C}} = \begin{pmatrix}\Delta v_{\mathrm{H}}^{\mathrm{C}} & \Delta v_{\mathrm{L}}^{\mathrm{C}}\end{pmatrix}^{\mathrm{T}}.$$

The transfer functions G^{C} from inputs Δu^{C} to outputs Δy are as follows:

$$\Delta y = \tilde{C}(sI - \tilde{A}^{\mathrm{C}})^{-1}\tilde{B}^{\mathrm{C}}\Delta u^{\mathrm{C}} = G^{\mathrm{C}}\Delta u^{\mathrm{C}} \tag{7}$$

where

$$G^{\mathrm{C}} = \begin{pmatrix}G_{11}^{\mathrm{C}} & G_{12}^{\mathrm{C}}\\ G_{21}^{\mathrm{C}} & G_{22}^{\mathrm{C}}\\ G_{31}^{\mathrm{C}} & G_{32}^{\mathrm{C}}\end{pmatrix} \tag{8}$$

$$G_{11}^{\mathrm{C}} = \frac{\left(s + \frac{r_{\mathrm{L}}}{L_{\mathrm{L}}}\right)s + \frac{D_{\mathrm{L}}'^2}{CL_{\mathrm{L}}}}{L_{\mathrm{H}}\mathit{\Phi}}$$

$$G_{12}^{\mathrm{C}} = \frac{-\frac{I_{\mathrm{L}}}{V_{\mathrm{link}}}\left(s + \frac{r_{\mathrm{L}}}{L_{\mathrm{L}}}\right) - \frac{D'_{\mathrm{L}}}{L_{\mathrm{L}}}}{CL_{\mathrm{H}}\mathit{\Phi}}$$

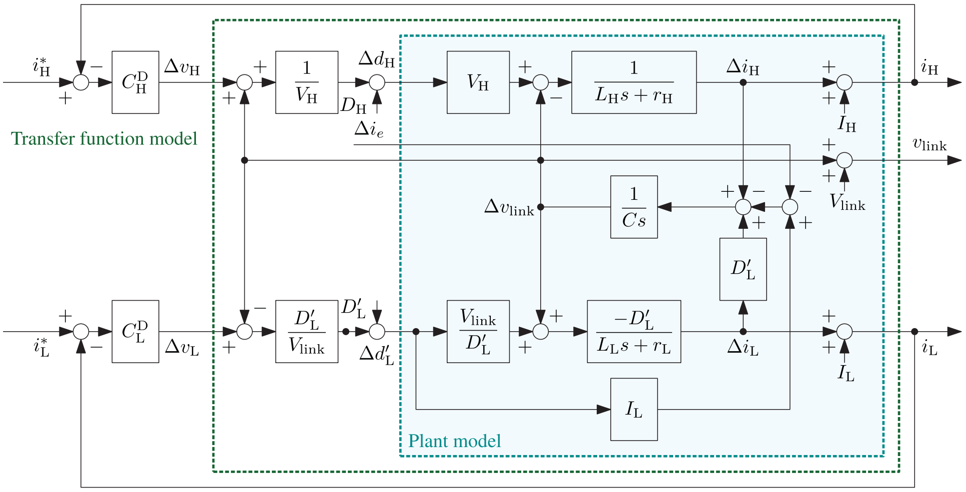

Fig. 4. Proposed control diagrams of the multiple converter system.

$$G_{21}^{\mathrm{C}} = \frac{D'_{\mathrm{L}}}{CL_{\mathrm{H}}L_{\mathrm{L}}\varPhi}$$

$$G_{22}^{\mathrm{C}} = \frac{-\left(s + \frac{r_{\mathrm{H}}}{L_{\mathrm{H}}}\right)\left(s + \frac{D'_{\mathrm{L}}I_{\mathrm{L}}}{CV_{\mathrm{link}}}\right) - \frac{1}{CL_{\mathrm{H}}}}{L_{\mathrm{L}}\varPhi}$$

$$G_{31}^{\mathrm{C}} = \frac{s + \frac{r_{\mathrm{L}}}{L_{\mathrm{L}}}}{CL_{\mathrm{H}}\varPhi}$$

$$G_{32}^{\mathrm{C}} = \frac{\frac{I_{\mathrm{L}}}{C}\left(s + \frac{r_{\mathrm{H}}}{L_{\mathrm{H}}}\right)\left(s - \frac{D'_{\mathrm{L}}V_{\mathrm{link}} - r_{\mathrm{L}}I_{\mathrm{L}}}{L_{\mathrm{L}}I_{\mathrm{L}}}\right)}{V_{\mathrm{link}}\varPhi}$$

$$\varPhi = s^3 + \left(\frac{r_{\mathrm{H}}}{L_{\mathrm{H}}} + \frac{r_{\mathrm{L}}}{L_{\mathrm{L}}}\right)s^2 + \left(\frac{r_{\mathrm{H}}r_{\mathrm{L}}}{L_{\mathrm{H}}L_{\mathrm{L}}} + \frac{D_{\mathrm{L}}'^2}{CL_{\mathrm{L}}} + \frac{1}{CL_{\mathrm{H}}}\right)s + \frac{r_{\mathrm{H}}D_{\mathrm{L}}'^2 + r_{\mathrm{L}}}{CL_{\mathrm{H}}L_{\mathrm{L}}}.$$

G_{32}^{C} is from Δv_{L} to v_{link}. The numerator of G_{32} has a nonminimum-phase zero [26]. This nonminimum-phase zero is the same as a single boost converter except for the coefficient [27]. G_{21}^{C} and G_{12}^{C} are not equal to zero, and these transfer functions are affected by another output.

III. PROPOSED CONTROL DESIGN BASED ON DECOUPLING AND COMPENSATION

This chapter first presents the proposed method for a 2×2 MIMO converter, and then Section III-B describes the method for a generalized m boost converter and n buck converter.

A. *Proposed MIMO Current Decoupling Control*

Fig. 4 represents the overall proposed controller of the proposed system. The next part is the current controller, which contains the proposed input decoupling method shown in this section. The green box of Fig. 4 can be seen that the response from the input to the output current becomes a first-order system by adding and subtracting Δv_{link} in each input, respectively. In other words, disturbance compensation is performed by voltage fluctuation. This can be expressed analytically as follows:

$$\Delta d = \begin{pmatrix} \frac{1}{V_{\mathrm{H}}}(\Delta v_{\mathrm{H}}^{\mathrm{D}} + \Delta v_{\mathrm{link}}) \\ \frac{D_{\mathrm{L}}}{V_{\mathrm{link}}}(\Delta v_{\mathrm{L}}^{\mathrm{D}} - \Delta v_{\mathrm{link}}) \end{pmatrix}. \tag{9}$$

Substituting (9) into (2), the proposed decoupled state-space representation (10) is given by

$$\frac{d}{dt}\Delta x = \tilde{A}^{\mathrm{D}}\Delta x + \tilde{B}^{\mathrm{D}}\Delta u^{\mathrm{D}} \tag{10}$$

$$\Delta y = \tilde{C}\Delta x$$

$$\tilde{A}^{\mathrm{D}} = \begin{pmatrix} \frac{r_{\mathrm{H}}}{L_{\mathrm{H}}} & 0 & 0 \\ 0 & -\frac{r_{\mathrm{L}}}{L_{\mathrm{L}}} & 0 \\ \frac{1}{C} & \frac{D'_{\mathrm{L}}}{C} & -\frac{D_{\mathrm{L}}I_{\mathrm{L}}}{CV_{\mathrm{link}}} \end{pmatrix}$$

$$\tilde{B}^{\mathrm{D}} = \begin{pmatrix} \frac{1}{L_{\mathrm{H}}} & 0 \\ 0 & -\frac{D'_{\mathrm{L}}}{L_{\mathrm{L}}} \\ 0 & -\frac{D'_{\mathrm{L}}I_{\mathrm{L}}}{CV_{\mathrm{link}}} \end{pmatrix}$$

$$\Delta u^{\mathrm{D}} = \begin{pmatrix} \Delta v_{\mathrm{H}}^{\mathrm{D}} & \Delta v_{\mathrm{L}}^{\mathrm{D}} \end{pmatrix}^{\mathrm{T}}.$$

The transfer function matrix from decoupled inputs Δu^{D} to outputs Δy is calculated as

$$\Delta y = \tilde{C}(sI - \tilde{A}^{\mathrm{D}})^{-1}\tilde{B}^{\mathrm{D}}\Delta u^{\mathrm{D}} = G^{\mathrm{D}}\Delta u^{\mathrm{D}} \tag{11}$$

where

$$G^{\mathrm{D}} = \begin{pmatrix} G_{11}^{\mathrm{D}} & G_{12}^{\mathrm{D}} \\ G_{21}^{\mathrm{D}} & G_{22}^{\mathrm{D}} \\ G_{31}^{\mathrm{D}} & G_{32}^{\mathrm{D}} \end{pmatrix} \tag{12}$$

$$G_{11}^{\mathrm{D}} = \frac{1}{L_{\mathrm{H}}s + r_{\mathrm{H}}}$$

$$G_{12}^{\mathrm{D}} = G_{21}^{\mathrm{D}} = 0$$

$$G_{22}^{\mathrm{D}} = -\frac{D'_{\mathrm{L}}}{L_{\mathrm{L}}s + r_{\mathrm{L}}}$$

$$G_{31}^{\mathrm{D}} = \frac{V_{\mathrm{link}}}{(L_{\mathrm{H}}s + r_{\mathrm{H}})\,(CV_{\mathrm{link}}s + D'_{\mathrm{L}}I_{\mathrm{L}})}$$
$$G_{32}^{\mathrm{D}} = \frac{D'_{\mathrm{L}}I_{\mathrm{L}}L_{\mathrm{L}}s + D'_{\mathrm{L}}(I_{\mathrm{L}}r_{\mathrm{L}} - D'_{\mathrm{L}}V_{\mathrm{link}})}{(L_{\mathrm{L}}s + r_{\mathrm{L}})\,(CV_{\mathrm{link}}s + D'_{\mathrm{L}}I_{\mathrm{L}})}.$$

The diagonal terms of G_{12}^{D} and G_{21}^{D} are zero. The currents are not influenced by other inputs. Note that G_{32}^{D} also has a nonminimum-phase zero as a SISO system because $D_{\mathrm{L}}V_{\mathrm{link}}$ is significantly larger than $r_{\mathrm{L}}I_{\mathrm{L}}$ in general application.

The green box of Fig. 4 shows the block diagram of the proposed current decoupling control, as discussed above. Installing the real system, the steady-state values of $D = (D_{\mathrm{H}} \quad D'_{\mathrm{L}})^T$ are added in Δd. The proposed method assumes that the first-order systems from Δu^{D} to Δy are in the diagonal terms. No interference from other input is shown for the off-diagonal terms $G_{12}^{\mathrm{D}} = G_{21}^{\mathrm{D}} = 0$.

B. Controller Design With Generalized Multiconverters

Discussing the above, we have described the modeling of the proposed method for the cases $m = 1$ boost converter and $n = 1$ buck converter, but it can be generalized to a state equation with $m + n + 1$ rows. The proposed current control method is dynamic decoupling and simple modeling sensing dc link voltage shown in (9). Furthermore, no additional controller design is required. At this point, the generalized decoupled controller design is easy to implement using Δd_{G} and Δd_{G} of ith and jth rows are defined with the voltage of the ith boost converter $V_{\mathrm{H}i}$ and the voltage of the jth buck converter $V_{\mathrm{L}j}$

$$\frac{\mathrm{d}}{\mathrm{d}t}x_{\mathrm{G}} = f_{\mathrm{G}}(x_{\mathrm{G}}) =$$
$$\frac{\mathrm{d}}{\mathrm{d}t}\begin{pmatrix} i_{\mathrm{H}1} \\ \vdots \\ i_{\mathrm{H}i} \\ \vdots \\ i_{\mathrm{H}n} \\ i_{\mathrm{L}1} \\ \vdots \\ i_{\mathrm{L}j} \\ \vdots \\ i_{\mathrm{L}m} \\ v_{\mathrm{link}} \end{pmatrix} = \begin{pmatrix} \frac{d_{\mathrm{H}1}}{L_{\mathrm{H}1}}V_{\mathrm{H}1} - \frac{r_{\mathrm{H}1}}{L_{\mathrm{H}1}}i_{\mathrm{H}1} - \frac{v_{\mathrm{link}}}{L_{\mathrm{H}1}} \\ \vdots \\ \frac{d_{\mathrm{H}i}}{L_{\mathrm{H}i}}V_{\mathrm{H}i} - \frac{r_{\mathrm{H}i}}{L_{\mathrm{H}i}}i_{\mathrm{H}i} - \frac{v_{\mathrm{link}}}{L_{\mathrm{H}i}} \\ \vdots \\ \frac{d_{\mathrm{H}n}}{L_{\mathrm{H}n}}V_{\mathrm{H}n} - \frac{r_{\mathrm{H}n}}{L_{\mathrm{H}n}}i_{\mathrm{H}n} - \frac{v_{\mathrm{link}}}{L_{\mathrm{H}n}} \\ -\frac{r_{\mathrm{L}1}}{L_{\mathrm{L}1}}i_{\mathrm{L}1} - \frac{d'_{\mathrm{L}1}}{L_{\mathrm{L}1}}v_{\mathrm{link}} + \frac{v_{\mathrm{link}}}{L_{\mathrm{L}1}} \\ \vdots \\ -\frac{r_{\mathrm{L}j}}{L_{\mathrm{L}j}}i_{\mathrm{L}j} - \frac{d'_{\mathrm{L}j}}{L_{\mathrm{L}j}}v_{\mathrm{link}} + \frac{v_{\mathrm{link}}}{L_{\mathrm{L}j}} \\ \vdots \\ -\frac{r_{\mathrm{L}m}}{L_{\mathrm{L}m}}i_{\mathrm{L}m} - \frac{d'_{\mathrm{L}m}}{L_{\mathrm{L}m}}v_{\mathrm{link}} + \frac{v_{\mathrm{link}}}{L_{\mathrm{L}m}} \\ \sum_{i=1}^{i=n}\frac{i_{\mathrm{H}i}}{C} + \sum_{j=1}^{j=m}\frac{d_{\mathrm{L}j}}{C}i_{\mathrm{L}j} - \frac{i_e}{C} \end{pmatrix}.$$

Applying the above equation in Section II-A is the same method

$$\frac{d}{dt}\Delta x_{\mathrm{G}} = \tilde{A_{\mathrm{G}}}\Delta x_{\mathrm{G}} + \tilde{B_{\mathrm{G}}}\Delta d_{\mathrm{G}} \tag{13}$$
$$\Delta y_{\mathrm{G}} = \tilde{C_{\mathrm{G}}}\Delta x_{\mathrm{G}} \tag{14}$$

where $\Delta x_{\mathrm{G}} = \Delta y_{\mathrm{G}}$

$$\tilde{A_{\mathrm{G}}} = \left(\frac{\partial f_{\mathrm{G}}}{\partial x_{\mathrm{G}k}}\right), \tilde{B_{\mathrm{G}}} = \left(\frac{\partial f_{\mathrm{G}}}{\partial d_{\mathrm{G}k}}\right)$$
$$\tilde{C_{\mathrm{G}}} = I$$
$$\Delta d_{\mathrm{G}} = \begin{pmatrix} d_{\mathrm{H}1}\cdots d_{\mathrm{H}i}\cdots d_{\mathrm{H}n} & d'_{\mathrm{L}1}\cdots d'_{\mathrm{L}j}\cdots d'_{\mathrm{L}m} \end{pmatrix}.$$

By performing the same operations Δd_{G} as in Section III-A, the following state equation is obtained:

$$\Delta d_{\mathrm{G}} = \begin{pmatrix} \frac{1}{V_{\mathrm{H}1}}(\Delta v_{\mathrm{H}1}^{\mathrm{D}} + \Delta v_{\mathrm{link}}) \\ \vdots \\ \frac{1}{V_{\mathrm{H}i}}(\Delta v_{\mathrm{H}i}^{\mathrm{D}} + \Delta v_{\mathrm{link}}) \\ \vdots \\ \frac{1}{V_{\mathrm{H}n}}(\Delta v_{\mathrm{H}n}^{\mathrm{D}} + \Delta v_{\mathrm{link}}) \\ \frac{D_{\mathrm{L}1}}{V_{\mathrm{link}}}(\Delta v_{\mathrm{L}1}^{\mathrm{D}} - \Delta v_{\mathrm{link}}) \\ \vdots \\ \frac{D_{\mathrm{L}j}}{V_{\mathrm{link}}}(\Delta v_{\mathrm{L}j}^{\mathrm{D}} - \Delta v_{\mathrm{link}}) \\ \vdots \\ \frac{D_{\mathrm{L}m}}{V_{\mathrm{link}}}(\Delta v_{\mathrm{L}m}^{\mathrm{D}} - \Delta v_{\mathrm{link}}) \end{pmatrix}. \tag{15}$$

The currents are decoupled by substituting the following (15) into (13) in the same manner of Section III-A

$$\frac{d}{dt}\Delta x_{\mathrm{G}} = \tilde{A_{\mathrm{G}}^{\mathrm{D}}}\Delta x_{\mathrm{G}} + \tilde{B_{\mathrm{G}}^{\mathrm{D}}}\Delta u_{\mathrm{G}}^{\mathrm{D}} \tag{16}$$
$$G_{\mathrm{G}}^{\mathrm{D}} = \frac{\Delta y_{\mathrm{G}}}{\Delta u_{\mathrm{G}}^{\mathrm{D}}} = \tilde{C_{\mathrm{G}}}(sI - \tilde{A_{\mathrm{G}}^{\mathrm{D}}})\tilde{B_{\mathrm{G}}^{\mathrm{D}}} \tag{17}$$
$$= \begin{pmatrix} G_{\mathrm{H}1}^{\mathrm{D}} & 0 & \cdots & & & & \\ 0 & \ddots & 0 & \cdots & & & \\ 0 & \cdots & G_{\mathrm{H}i}^{\mathrm{D}} & 0 & \cdots & & \\ 0 & \cdots & & \ddots & 0 & \cdots & \\ 0 & \cdots & & 0 & G_{\mathrm{L}j}^{\mathrm{D}} & 0 & \cdots \\ 0 & \cdots & & & 0 & \ddots & 0\cdots \\ G_{\mathrm{V}1}^{\mathrm{D}} & \cdots & G_{\mathrm{V}i}^{\mathrm{D}} & \cdots & G_{\mathrm{V}n+j}^{\mathrm{D}} & \cdots & G_{\mathrm{V}n+m}^{\mathrm{D}} \end{pmatrix}.$$

All the off-diagonal terms of the transfer function G_{G} except for the final voltage term, v_{link}, are zero; no mutual interference is theoretically derived.

Increasing the number of converters leads to an increase in the number of controllers, which grows exponentially in noninterference control based on general MIMO theory. However, the implementation of the proposed controllers only involves the addition and subtraction of terms that measure the dc link voltage, as shown in (15). Therefore, the increase in controller complexity is linear.

IV. EXPERIMENTAL RESULTS

In this section, the improvement of decoupling, stability analysis, and tracking performance is validated. Section IV-B confirms the independence of each input shown in (C1), Section IV-C shows the stability corresponding to (C2), and Section IV-D examines the tracking performance in (C3). These experiments can be easily extended to $m \times n$ converters.

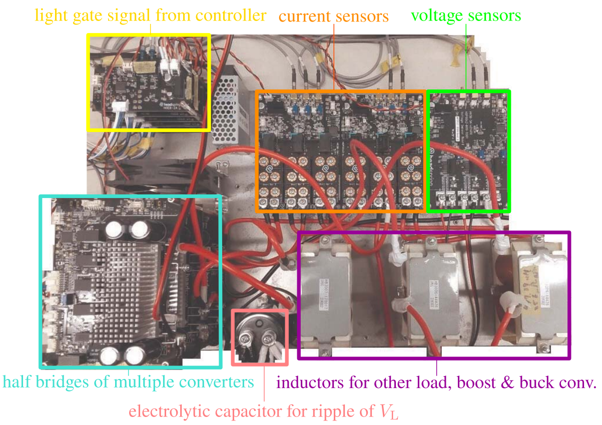

Fig. 5. Experimental setup of the system.

TABLE I
EXPERIMENTAL PARAMETERS OF THE BENCH SYSTEM

Parameter	Value	Parameter	Value
L_H	1.23 mH	r_H	0.328 Ω
L_L	438 μH	r_L	0.206 Ω
C_{link}	712 nF		
V_H	200 V	V_L	100 V
Dead time	500 ns	f_{sw}	20 kHz

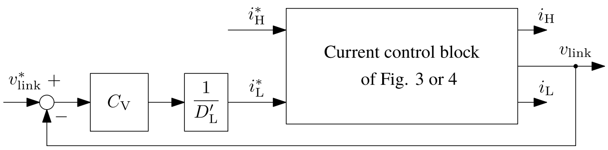

Fig. 6. Block diagram of the experiment for the closed-loop system identification.

A. Experimental Setup

Fig. 5 illustrates the experimental setup used in the experiment. The circuit configurations are shown in Fig. 2(b). Table I summarizes the circuit parameters of the system. The circuit parameters of the system are measured at the same converter carrier frequency f_{sw} of 20 kHz. The dc link capacitor consists of a combination of electrolytic capacitors and ceramic capacitors to reduce the switching surges of the converters. The controller is used for MWPE4-PEV of PE-Expert4 made by Myway Plus in all experiments. Calculation period is the same carrier frequency f_{sw}. The controller is installed one sample delay of 50 μs, which is a classic implementation. The data also collect the analog-to-digital (AD) converter of MWPE4-PEV by using the sensor boards, which consist of F02P050S05 L made by Tamura Corp, whose conversion time is 500 ns.

B. System Identification of the MIMO Current Decoupling Control System

TABLE II
CONTROLLER CONDITIONS USED IN SYSTEM IDENTIFICATION

Parameter	Value	Parameter	Value
ω_H	21 Hz	ω_L	21 Hz
ω_V	7 Hz		
I_H^*	4 A	V_{link}^*	160 V

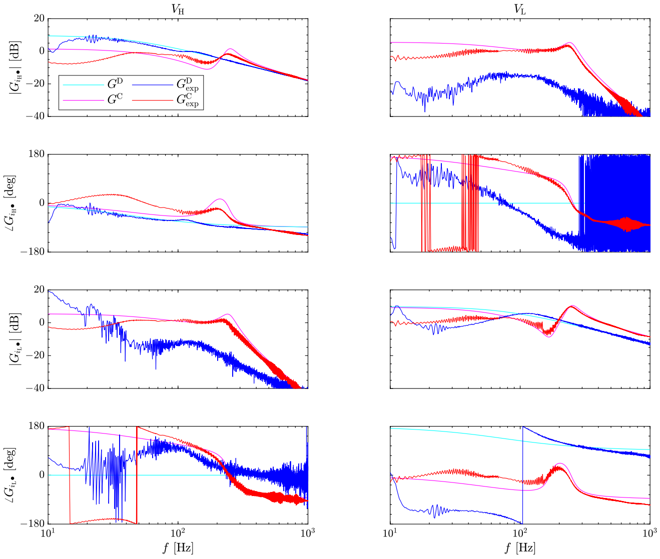

Fig. 7. Bode diagrams of the system w/o and w/ decoupling in state-space model G^C in (8) and G^D in (13), frequency response data w/o and w/ decoupling G^C_{exp} and G^D_{exp}.

Fig. 6 shows block diagram of the overall control for system identification. System identification is often performed using an open loop. However, in this article, system identification with weak feedback was employed to facilitate comparison with a theoretical transfer functions (8) and (13) at a fixed operating point. This article installed the voltage controller at the lower boost converter. The closed-loop system identification is separately done by the charp signal V_C from 1 to 1500 Hz adding each input Δv as shown in Figs. 3 or 4. PI gains of the current controller are designed by pole placement

$$C_H^C = C_H^D = K_{PH} + \frac{K_{IH}}{s} = 2\omega_H L_H - R_H + \frac{\omega_H^2 L_H}{s}$$

$$C_L^C = C_L^D = K_{PL} + \frac{K_{IL}}{s} = \frac{2\omega_L L_L - R_L}{D'_L} + \frac{\omega_H^2 L_H}{D'_L s}. \quad (18)$$

Here, ω_H and ω_L are angular frequencies of the pole. The pole placement method is more stable than the pole-zero cancellation even when there is a modeling error in the control plant. The boost converter contains the D'_L but the conventional method included D'_L before the duty input d'_L; this coefficient cancels out and the gain design is the same as that of the buck converter. C_V is the voltage PI controller to maintain the dc link voltage, whose gain is also designed by pole placement

$$C_V = K_{PV} + \frac{K_{IV}}{s} = 2\omega_V C + \frac{\omega_V^2 C}{s}. \quad (19)$$

Table II summarizes the control parameters for the system identification of the conventional and proposed methods in the currents. Mentioned above, the system identification with weak feedback was employed to avoid affecting.

Fig. 7 shows the Bode diagrams of the proposed system with the conventional method and the proposed decoupling method.

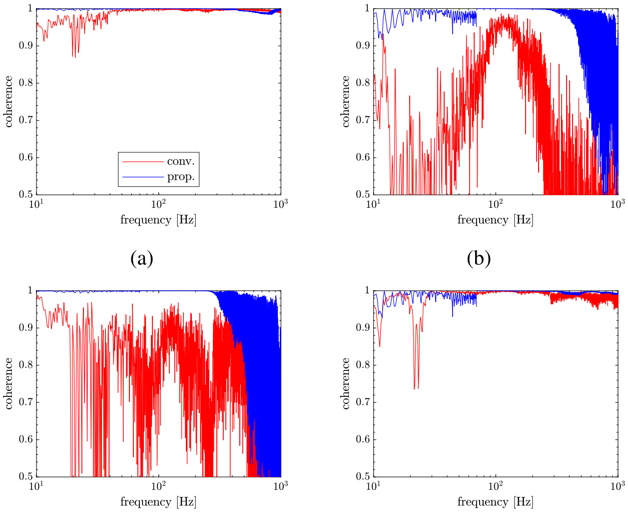

(a) (b)

(c) (d)

Fig. 8. Coherence of the experimental identification between inputs and outputs. (a) From v_H to i_H. (b) From v_H to i_L. (c) From v_L to i_H. (d) From v_L to i_L.

The experimental frequency response data contain the sensor noise, error, quantizations, and controller delay. The lower frequency range is not matched due to the internal impedance of the experimental voltage source. These differences are due to the input impedance of the constant voltage sources V_H and V_L. However, the controller can be suppressed by the higher frequency feedback loop. The conventional experimental result fits the simulation result of the resonant and antiresonant frequency in each input and output except for the lower frequency range. Besides, the experimental proposed method matches the model-based calculation of (13) in the diagonal elements. The off-diagonal elements of the experimental proposed method remain around −20 dB since the measuring noise contains the outputs.

Fig. 8 plots the coherence of the system identification. Coherence is a function that takes values between 0 and 1 and has the property of taking a value of 1 when two signals are perfectly linear. By utilizing this property and checking the value of the coherence function for each frequency of the input or output data used in the frequency response measurement, it is possible to determine whether the frequency response data have high linearity. The off-diagonal terms of the coherence in the conventional method are lower compared to the diagonal terms, which is due to the lower output signal. However, the diagonal terms exhibit high coherence and good agreement with the model, allowing for the simultaneous acquisition of data for the off-diagonal terms.

Relative gain array (RGA) is a useful tool in practical applications and provides a measure of interaction [26]. RGA Λ is calculated as

$$\Lambda = G \circ (G^{-1})^T \tag{20}$$

$$\Lambda_{ij} = \lambda_{ij} = [G]_{ij}[G^{-1}]_{ji}.$$

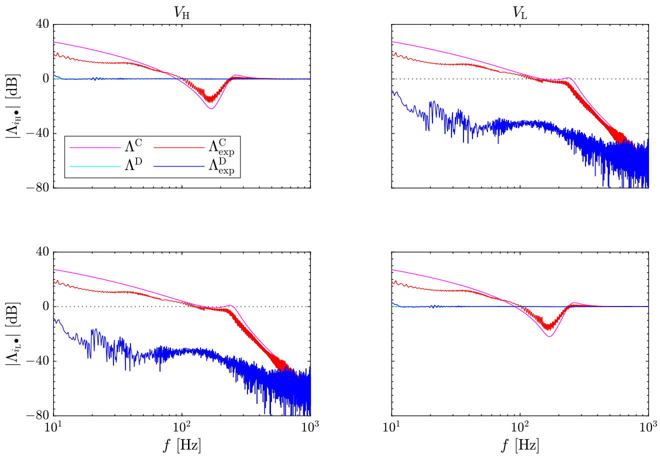

Fig. 9. RGA of the model-based and experimental results with conventional and decoupled methods, G^C, G^D, $G^\mathrm{C}_\mathrm{exp}$, and $G^\mathrm{D}_\mathrm{exp}$, respectively.

Here, "$\circ$" denotes Hadamard product, which means element-by-element multiplication. RGA is independent of input and output scaling.

Fig. 9 shows the RGA of the model-based and experimental results with the conventional and decoupled methods. Note that dominant input and output pairs have 0 dB of RGA and other pair is $-\infty$dB; in other words, they decouple. The conventional experimental results are the same as the model-based calculations except for the lower frequencies. Λ_{11} and Λ_{22} of the model-based decoupling method are 0 dB, and the off-diagonal terms are not displayed since the interrelations are extremely low in the all-frequency range shown in (13), respectively. The experimental decoupling results show similar trend to the model-based result. From the above results, the proposed method achieved the decoupling of currents in the system identification.

C. MIMO Nyquist Stability Analysis With Experimental Frequency Response Data

The Nyquist diagram is one of the determining stability and is performed by plotting the vector locus of the open-loop transfer function L using the transfer functions G and controller C

$$L(j\omega) = G(j\omega)C(j\omega). \tag{21}$$

The MIMO system may become unstable due to interactions between inputs, even if each individual SISO system is stable. MIMO stability is assessed using the direct Nyquist array (DNA) method with generalized Gershgorin bands. By applying the DNA theorem, the stability condition is satisfied when the band locus (which is called a generalized Gershgorin band) drawn by a circle with radius r_{gq} shown in (22), centered on the qth diagonal element L_{qq} of L at all frequencies, turns around the critical point the same number of times as the number of unstable poles of the target plant G

$$r_{gq}(\mathrm{j}\omega_k) = \lambda(\mathrm{j}\omega_k)|L_{qq}(\mathrm{j}\omega_k)| \tag{22}$$

$$\text{where} \quad \lambda(\mathrm{j}\omega_k) = \max \operatorname{eig}\{M(\mathrm{j}\omega_k)\}$$

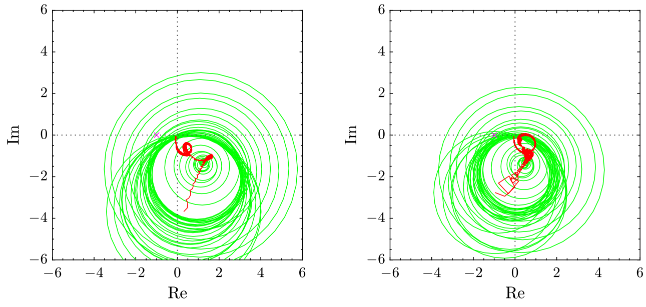

(a) (b)

Fig. 10. Nyquist diagrams with generalized Gershgorin bands of experimental conventional current control from experimental frequency response data $\exp G^{\mathrm{C}}$ of Fig. 7 shown in Fig. 3. Generalized Gershgorin bands plotted at 50 points of the same intervals on a log scale from 10 Hz to 1 kHz. (a) From $V_{\mathrm{H}}^{\mathrm{C}}$ to Δi_{H}. (b) From $V_{\mathrm{L}}^{\mathrm{C}}$ to Δi_{L}.

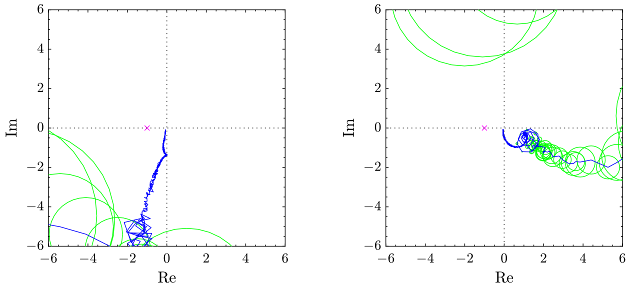

(a) (b)

Fig. 11. Nyquist diagrams with generalized Gershgorin bands of the proposed current control from experimental frequency response data $\exp G^{\mathrm{D}}$ shown in Fig. 4. Generalized Gershgorin bands are plotted at 50 points of the same intervals on a log scale from 10 Hz to 1 kHz. (a) from $\Delta v_{\mathrm{H}}^{\mathrm{D}}$ to Δi_{H}. (b) from $\Delta v_{\mathrm{L}}^{\mathrm{D}}$ to Δi_{L}.

TABLE III
PARAMETERS OF PI CONTROL IN THE NYQUIST PLOT SHOWN IN (18)

Parameter	Value	Parameter	Value
ω_{H}	100 Hz	ω_{L}	100 Hz

$$M(\mathrm{j}\omega) = \begin{cases} 0 & (p = q) \\ \frac{G_{ij}(\mathrm{j}\omega_k)}{G_{ii}(\mathrm{j}\omega_k)} & (p \neq q) \end{cases}.$$

Here, eig is an eigenvalue calculation of the matrix. In a normal case, the generalized Gershgorin bands do not include the point of (−1,0j) on the Nyquist diagram, the system satisfies a MIMO stability condition with the interaction between each input.

Figs. 10 and 11 illustrate the Nyquist diagrams of open-loop frequency response data from voltage command value to output current, respectively. These calculations were done from experimental transfer function data G, as shown in Fig. 7, including a sensor noise, error, quantizations, and controller delay and the ideal PI controllers C_{H} and C_{L} obtained by (18) with the parameter of the angular frequency shown in Table III. The black lines mean the SISO Nyquist plots of the current control systems. The open-loop frequency response of each axis may move within the radius of the generalized Gershgorin bands at each frequency point on the Nyquist diagram when MIMO systems interact between each axis. The conventional current control method in Fig. 10 is stable, as shown in the SISO Nyquist plots. However, the generalized Gershgorin bands conclude that the overall current control system may be unstable because these bands contain $(-1, \mathrm{j}0)$ in each axis. In contrast, the proposed current control method in Fig. 11 is stable from both the SISO Nyquist diagrams and the generalized Gershgorin bands, but the band remains a width due to sensor noise and dc link voltage sample delay. The smaller generalized Gershgorin bands depict the better decoupling performance with the proposed method. Although the generalized Gershgorin band is a sufficient MIMO stability condition, the MIMO stability guarantee is necessary to analyze the multiple converter applications.

The proposed method is only used for the dc link voltage Δv_{link} and does not use the circuit parameter, because Δv_{link} contains the information of circuit parameters shown in Fig. 4. In other words, the circuit parameter and steady-state condition

TABLE IV
EXPERIMENTAL PARAMETERS OF THE STEP RESPONSES

Parameter	Value	Parameter	Value
V_e	200 V	V_{V}	100 V
L_e	404 μH	r_e	0.422 Ω
L_{V}	447 μ H	r_{V}	0.253 Ω
ω_{H}	21 Hz	ω_{L}	21 Hz
ω_{VC}	21 Hz	ω_{VV}	7 Hz
ω_{e}	800 Hz		
Initial condition of the command value			
I_{H}^*	4 A	I_{L}^*	5 A
I_e^*	0 A	V_{link}^*	160 V

Other parameter are in Table I.

TABLE V
COMPARISON BETWEEN CONVENTIONAL AND PROPOSED METHOD

Step		maximum error			converged time [ms]		
		$i_{\mathrm{H}}[A]$	$i_{\mathrm{L}}[A]$	v_{link} [V]	i_{H}	i_{L}	v_{link}
i_{H}	conv.	0.7	1.4	9.4	70	22	40
	prop.	0.3	0.4	12	12	19	35
i_{L}	conv.	8.1	1.0	9.5	65	50	60
	prop.	1.6	NA	11	3	20	60
i_e	conv.	1.2	1.8	12	60	40	60
	prop.	0.3	1.1	16	4	50	60
v_{link}	conv.	0.6	1.1	3.1	60	60	60
	prop.	0.1	0.3	2.5	5	20	35

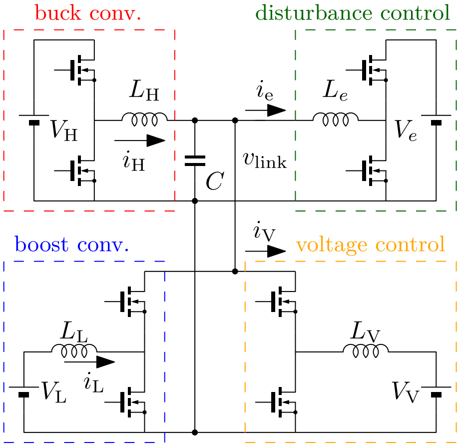

Fig. 12. Circuit diagram of the experiment for the step response.

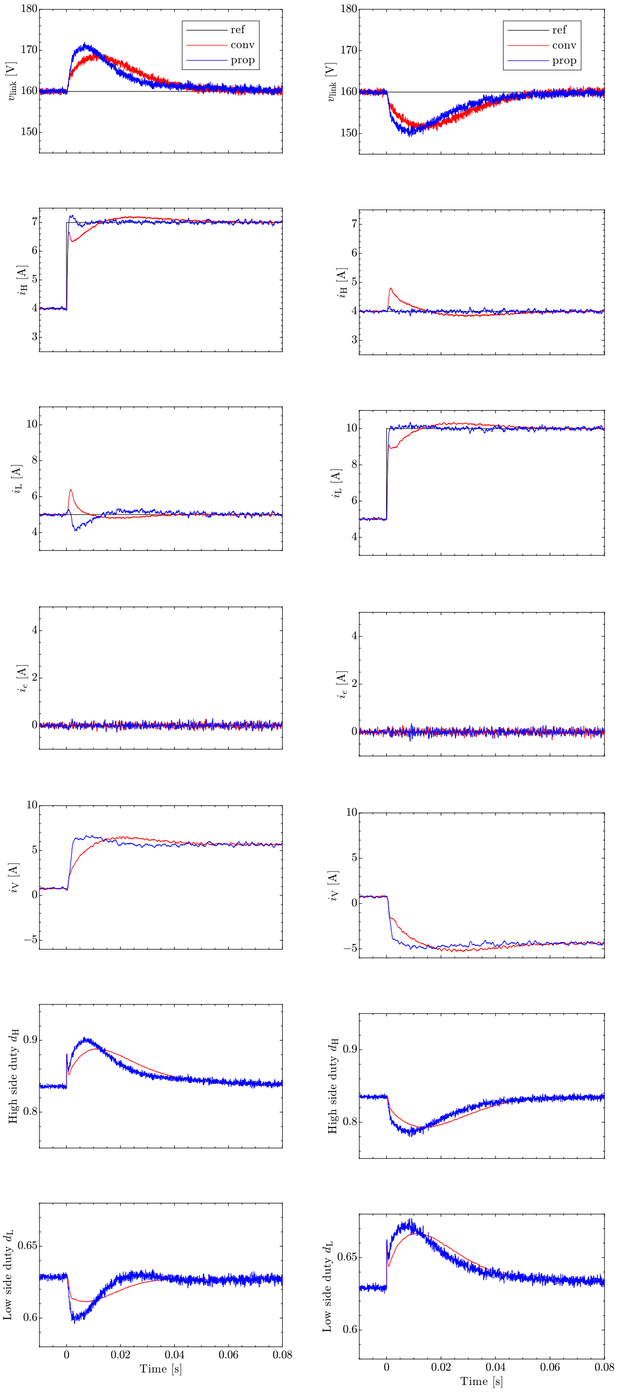

(a) (b)

Fig. 13. Current step responses of the system with Fig. 12 when $I_e = 0$. (a) i_{V}, i_{H}, i_{L}, i_e, i_{V}, d_{H}, and d_{L} of i_{H}^* step from 4 to 7 A. (b) i_{V}, i_{H}, i_{L}, i_e, i_{V}, d_{H}, and d_{L} of i_{L}^* step from 5 to 10 A.

are only used for plotting the Bode. For the reasons stated above, the proposed method is not affected by changes in the circuit parameters.

D. Tracking Performance in Various Step Responses

This section examines the step response of the system. The four cases of the experiments were done, which are i_{H}, i_{L}, i_e, and v_{link} of the step responses to test the effects of the disturbance current and voltage.

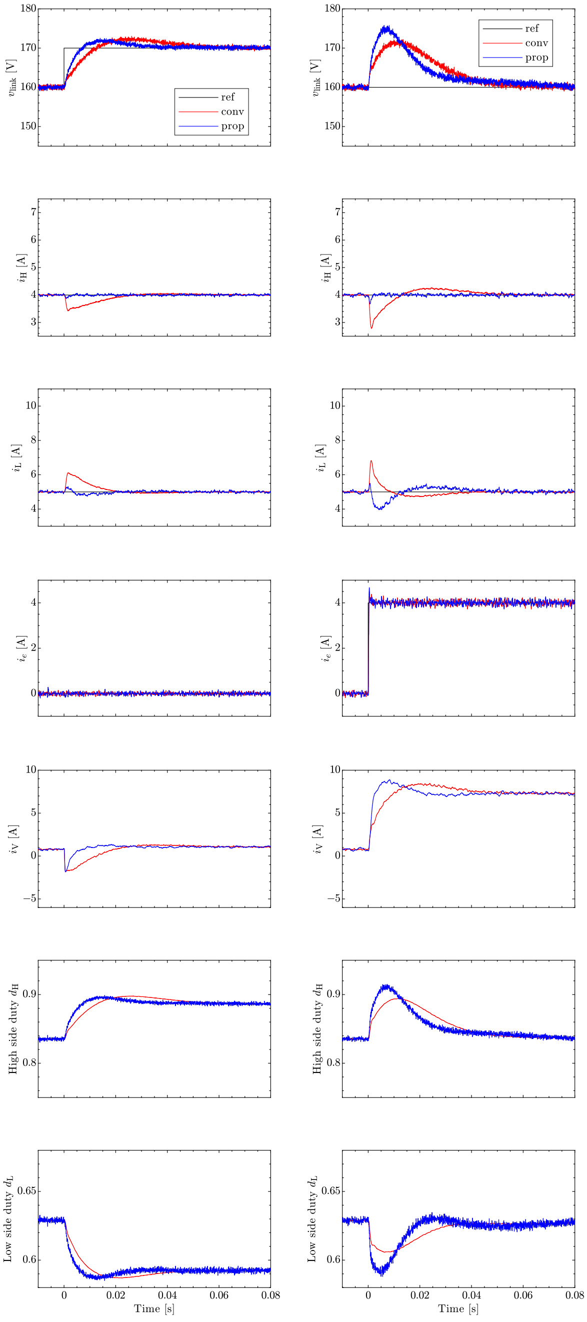

(a) (b)

Fig. 14. Disturbance step responses of the system with Fig. 12 when I_{H}^*=4 A and I_{L}^*= 5 A. (a) i_{V}, i_{H}, i_{L}, i_e, i_{V}, d_{H}, and d_{L} of v_{link}^* step from 160 to 170 V. (b) i_{V}, i_{H}, i_{L}, i_e, i_{V}, d_{H}, and d_{L} of i_e^* step from 0 to 4 A.

Fig. 12 shows the experimental circuit diagram of the system. The system consists of four converters. Two converters are the proposed system, which is a boost converter and a buck converter. Other converters are a current disturbance converter and a voltage controlled converter. The parameters of the system are listed in Table IV. The controller of the current disturbance converter is designed in the same equations as (18) except for angular frequency. The angular frequency of the current disturbance converter ω_e is 800 Hz, and the controller is installed with the proposed method for the sake of following the disturbance current command value. The voltage converter controller is also designed according to (19), and the current controller is the same in the lower boost converter.

Fig. 13 shows the current step responses of the system. The overshoot or undershoot currents and settling time are higher and longer than the conventional method in both current step responses in Fig. 13(a) and (b). The dc link voltage also shows shorter convergence in Fig. 13, but the overshoot or undershoot voltage is higher than the conventional method, which results from the excessive injection current to the dc link capacitors compared to the conventional method. The fluctuation of the i_{L} in Fig. 13(a) is observed for the linearizing error of the state-space equations and the remaining low frequency response of Fig. 7. These phenomena are also observed in higher response in i_{V}. The duty command of the proposed method has resulted in the compensation of the dc link voltage. However, the output currents show little fluctuation of the converged state compared to the duty noise. To eliminate the fluctuation, a noise filter should be implemented after the voltage sensor considering the delay. This delay may reduce the effectiveness of active decoupling and affect stability and characteristics. Even in such cases, stability and characteristics can be evaluated by verifying the Bode diagram and Nyquist diagram shown in Sections IV-B and IV-C. The proposed method is decoupled between each current; for this reason, the converged time of the currents and voltage is short.

Figs. 14 shows the disturbance step responses of the system. The overshoot currents i_{H} and i_{L} are significantly reduced compared to the conventional method. The converged time of the currents and the dc link voltage is also decreased for the same reason as in Fig. 13.

Table V summarizes the comparisons between the conventional and the proposed method. Both the converged time and overshoot or undershoot of the currents decrease in all step responses. Also, the converged time of the voltages is shorter than the conventional method due to faster currentt responses.

V. CONCLUSION

This article has proposed multiple converters connecting to the same dc link voltage. First of all, the dynamic current decoupling method of the MIMO system has been proposed. The model-based analysis concludes that the first-order systems were obtained by compensating the dc link voltage at the inputs. The proposed method only uses the dc link voltage and does not use the system parameters. The bench system has been tested to verify the decoupling performance by the Bode plots, Nyquist plots, and step response. The experimental Bode diagrams obtained by system identification confirmed that the conventional and proposed methods were consistent with the analytical results. Furthermore, the proposed method suppresses the interference of off-diagonal terms by approximately -20 dB. In addition, the RGA calculation from the experimental Bode diagrams confirmed that the diagonal terms were almost linear and the off-diagonal terms were decoupled by -40 dB. Nyquist plots have also confirmed that the conventional control might deteriorate the stability for the Gershgorin bands analysis, and the proposed method is stable in both the SISO Nyquist diagrams and the Gershgorin bands. Step responses have also verified that the proposed control suppresses the overshoot voltage and currents compared with the conventional control and suppresses the converged time faster than the conventional control. Future work would remain on the periodic fluctuation and the large current change resulting from grid current, as well as designing the voltage controller considering the grid current, and the high-frequency converter used in gallium nitride (GaN) devices.

REFERENCES

[1] X. Li, M. Wang, W. Jiang, C. Dong, Z. Xu, and X. Wu, "Toward large-signal stabilization of interleaved floating multilevel boost converter-enabled high-power dc microgrids supplying constant power loads," *IEEE Trans. Ind. Electron.*, vol. 71, no. 1, pp. 857–869, Jan. 2024.

[2] M. A. Hassan et al., "DC shipboard microgrids with constant power loads: A review of advanced nonlinear control strategies and stabilization techniques," *IEEE Trans. Smart Grid*, vol. 13, no. 5, pp. 3422–3438, Sep. 2022.

[3] A. Emadi, A. Khaligh, C. Rivetta, and G. Williamson, "Constant power loads and negative impedance instability in automotive systems: Definition, modeling, stability, and control of power electronic converters and motor drives," *IEEE Trans. Veh. Technol.*, vol. 55, no. 4, pp. 1112–1125, Jul. 2006.

[4] S.-Y. Chen and C.-H. Chang, "Optimal power flows control for home energy management with renewable energy and energy storage systems," *IEEE Trans. Energy Convers.*, vol. 38, no. 1, pp. 218–229, Mar. 2023.

[5] A. Sangswang and M. Konghirun, "Optimal strategies in home energy management system integrating solar power, energy storage, and vehicle-to-grid for grid support and energy efficiency," *IEEE Trans. Ind. Appl.*, vol. 56, no. 5, pp. 5716–5728, Sep./Oct. 2020.

[6] J. Engel, T. Schmitt, T. Rodemann, and J. Adamy, "Hierarchical economic model predictive control approach for a building energy management system with scenario-driven EV charging," *IEEE Trans. Smart Grid*, vol. 13, no. 4, pp. 3082–3093, Jul. 2022.

[7] E. Oh and S.-Y. Son, "Shared electrical energy storage service model and strategy for apartment-type factory buildings," *IEEE Access*, vol. 7, pp. 130340–130351, 2019.

[8] S. Nakahara et al., "Development of dual active bridge dc-dc converter to achieve high efficiency in wide voltage and load range and application to V2H systems," *IEEJ J. Ind. Appl.*, vol. 13, no. 4, pp. 475–488, 2024.

[9] T. Ericsen, N. Hingorani, and Y. Khersonsky, "PEBB - power electronics building blocks from concept to reality," in *Proc. Rec. Conf. Papers - IEEE Ind. Appl. Soc. 53rd Annu. Petroleum Chem. Ind. Conf.*, 2006, pp. 1–7.

[10] A. R. Iyer, R. P. Kandula, R. Moghe, J. E. Hernandez, F. C. Lambert, and D. Divan, "Validation of the plug-and-play AC/AC power electronics building block (AC-PEBB) for medium-voltage grid control applications," *IEEE Trans. Ind. Appl.*, vol. 50, no. 5, pp. 3549–3557, Sep./Oct. 2014.

[11] L. Xue et al., "Modular power electronics approach for high-power dynamic wireless charging system," *IEEE Trans. Transport. Electrific.*, vol. 10, no. 1, pp. 976–988, Mar. 2024.

[12] A. Deshpande, Y. Chen, B. Narayanasamy, Z. Yuan, C. Chen, and F. Luo, "Design of a high-efficiency, high specific-power three-level t-type power electronics building block for aircraft electric-propulsion drives," *IEEE Trans. Emerg. Sel. Topics Power Electron.*, vol. 8, no. 1, pp. 407–416, Mar. 2020.

[13] K. Yamanokuchi, H. Watanabe, and J.-I. Itoh, "Distributed control method for power conversion system with series-connected autonomous modular converters," *IEEE Trans. Power Electron.*, vol. 38, no. 12, pp. 15242–15252, Dec. 2023.

[14] H. Watanabe, K. Yamanokuchi, Y. Ikeda, Y. Takahashi, and J.-i. Itoh, "Universal smart power module (USPM) for carbon neutral society," *IEEE Trans. Ind. Appl.*, vol. 60, no. 2, pp. 3411–3417, Mar./Apr. 2024.

[15] B. A. Martınez-Treviño, A. E. Aroudi, H. Valderrama-Blavi, A. Cid-Pastor, E. Vidal-Idiarte, and L. Martinez-Salamero, "PWM nonlinear control with load power estimation for output voltage regulation of a boost converter with constant power load," *IEEE Trans. Power Electron.*, vol. 36, no. 2, pp. 2143–2153, Feb. 2021.

[16] M. A. Hassan, C.-L. Su, F.-Z. Chen, and K.-Y. Lo, "Adaptive passivity-based control of a DC–DC boost power converter supplying constant power and constant voltage loads," *IEEE Trans. Ind. Electron.*, vol. 69, no. 6, pp. 6204–6214, Jun. 2022.

[17] M. Abdolahi, J. Adabi, and S. Y. M. Mousavi, “An adaptive extended Kalman filter with passivity-based control for DC-DC converter in DC microgrids supplying constant power loads,” *IEEE Trans. Ind. Electron.*, vol. 71, no. 5, pp. 4873–4882, May 2024.

[18] B. He, W. Chen, C. Zhang, Y. Yuan, and C. Zhang, “Impedance specifications for stability design of grid-connected DC distribution power systems,” *IEEE Trans. Ind. Electron.*, vol. 71, no. 6, pp. 5830–5843, Jun. 2024.

[19] Y. Mitsugi and J. Baba, “Phaser-based transfer function analysis of power synchronization control instability for a grid forming inverter in a stiff grid,” *IEEE Access*, vol. 11, pp. 42146–42159, 2023.

[20] H. Fuse et al., “Frequency-domain analysis and joint torque vibration suppression control on two-input-two-output torque difference amplification motor drive system of electrified vehicles,” *SAE Int. J. Veh. Dyn., Stability, NVH*, vol. 7, no. 3, pp. 313–328, Jun. 2023.

[21] W. Ohnishi, A. Hirata, R. Shibatsuji, and T. Yamaguchi, “Fast and precise temperature control for a semiconductor vertical furnace via heater-cooler integration,” *IEEE Trans. Semicond. Manuf.*, vol. 36, no. 2, pp. 197–204, May 2023.

[22] M. van Dael et al., “Online decoupling of the time-varying longitudinal feedback loops for improved performance in advanced virgo plus*,” *Classical Quantum Gravity*, vol. 41, no. 21, Oct. 2024, Art. no. 215008.

[23] J. Wang, X. Qiao, L. Li, R. Wang, and H. Qin, “Decoupling control strategy of three-port DC–DC converter based on model prediction,” *Sci. Rep.*, vol. 14, no. 1, 2024, Art. no. 26478.

[24] O. E. Oyewole and K. H. Ahmed, “Comparative analysis of decoupling control methods for multiport-isolated bidirectional DC-DC converter with hydrogen storage system integration,” in *Proc. 11th Int. Conf. Smart Grid*, 2023, pp. 1–8.

[25] G. Garraffa, A. Accetta, M. Luna, M. Pucci, F. Alonge, and A. Sferlazza, “Indirect sliding mode control of a MIMO modular converter for dc microgrids: A ROV case study,” in *Proc. IEEE Energy Convers. Congr. Expo.*, 2024, pp. 3659–3664.

[26] S. Skogestad and I. Postlethwaite, *Multivariable Feedback Control*, 2nd ed. U.S.: Wiley, 2005.

[27] S. Miyoshi, W. Ohnishi, T. Koseki, and M. Sato, “Output voltage precise tracking control for boost converters based on noncausal and nonlinear feedforward control,” *IEEJ J. Ind. Appl.*, vol. 12, no. 6, pp. 1114–1126, 2023.

Toshiyuki Fujita (Member, IEEE) received the B.S. degree in electrical engineering, the M.S. degree in physical electronics, and the Ph.D. degree in electrical and electronic engineering from the Tokyo Institute of Technology, Meguro, Japan, in 2008, 2010, and 2017, respectively.

Since 2014, he has been with Technova Inc., Tokyo, Japan. From 2010 to 2014, He was with Panasonic Corporation, Osaka, Japan. In 2019, he joined the University of Tokyo, Chiba, Japan, as a Project Assistant Professor, and since 2021, he has been a Project Lecturer. His research interests include WPT systems for electric vehicles, ac/dc converters, and their control methods.

Dr. Fujita is a Member of Institute of Electrical Engineers of Japan, Society of Automotive Engineers of Japan, and Japan Society of Applied Physics.

Masahiro Mae (Member, IEEE) received the B.E. degree in electrical and electronic engineering, the M.S. degree in advanced energy, and the Ph.D. degree in electrical engineering and information systems from The University of Tokyo, Tokyo, Japan, in 2018, 2020, and 2023, respectively.

He is currently an Assistant Professor with the Department of Electrical Engineering and Information Systems, Graduate School of Engineering, The University of Tokyo. His research interests include multivariable control and data-driven optimization for industrial mechatronics and energy systems.

Dr. Mae is a Member of Institute of Electrical Engineers of Japan, Society of Instrument and Control Engineers, Society of Automotive Engineers of Japan, and Japan Society of Energy and Resources.

Hiroshi Fujimoto (Fellow, IEEE) received the Ph.D. degree in electrical engineering from the Department of Electrical Engineering, The University of Tokyo, Kashiwa, Japan, in 2001.

In 2001, he joined the Department of Electrical Engineering, Nagaoka University of Technology, Niigata, Japan, as a Research Associate. From 2002 to 2003, he was a Visiting Scholar with the School of Mechanical Engineering, Purdue University, West Lafayette, IN, USA. In 2004, he joined the Department of Electrical and Computer Engineering, Yokohama National University, Yokohama, Japan, as a Lecturer, and became an Associate Professor in 2005. He was an Associate Professor with The University of Tokyo from 2010 to 2020 and since 2021, he has been a Professor. His interests include control engineering, motion control, nanoscale servo systems, electric vehicle control, motor drive, visual servoing, and wireless power transfer.

Dr. Fujimoto was the recipient of the Best Paper Award from the IEEE Transactions on Industrial Electronics in 2001 and 2013, Isao Takahashi Power Electronics Award in 2010, Best Author Prize of SICE in 2010, the Nagamori Grand Award in 2016, First Prize Paper Award for IEEE Transactions on Power Electronics in 2016, and IEEJ Industry Applications Society Distinguished Transaction Paper Award in 2018 and 2023. He is also a Member of the SICE, RSJ, and JSAE. Since 2022, He has been a Senior Editor for IEEE/ASME TRANSACTIONS ON MECHATRONICS and an Associate Editor for the *IEEE Industrial Electronics Magazine* since 2006. Since 2022, he has been a Chairperson of the JSAE Technology Board and was a past Chairperson of the IEEE/IES Technical Committee on Motion Control from 2012 to 2013 and the JSAE vehicle electrification committee from 2014 to 2020.

Michihiro Nakagawa received the B.S. and M.S. degrees in electrical engineering from Ritsumeikan University, Kyoto, Japan, in 2007 and 2009, respectively.

Since April 2009, he has been with DAIKIN INDUSTRIES, Ltd., Settsu, Japan. He works on the development of motors for air conditioner equipment.

Yoshiki Yasuda received the B.E. and M.E. degrees in electrical and electronic systems engineering from Osaka Prefecture University, Sakai, Japan, in 2002 and 2004, respectively.

Since 2004, he has been with DAIKIN INDUSTRIES, Ltd., Settsu, Japan. He works on the development of motors for air conditioners and hydraulic equipment.

Akio Yamagiwa received the B.E. and M.E. degrees in electrical engineering from Toyama University, Toyama, Japan, in 1988 and 1990, respectively.

Since 1990, he has been with DAIKIN INDUSTRIES, Ltd., Settsu, Japan. He works on the development of motors for air conditioners and hydraulic equipment. He was a Senior Researcher from 2002 to 2011, a Chief Engineer from 2012 to 2022, and became an Executive Engineer from 2023. He was a General Manager with the Technology Research Association of Magnetic Materials for High Efficiency Motors from 2012 to 2017 and since 2018, he has been a Chief Researcher.

Mr. Yamagiwa was the recipient of the IEEJ Technical Development Award in 1998. He is a Member of the Japan Society of Mechanical Engineers. He is a President of the Japan Institute of Power Electronics from 2023.